Supporting Information

A non-percolating interfacial microcapacitor architecture decouples polarization enhancement from leakage suppression in humidity-tolerant polymer films

Qisheng Shao[a,†], *Wei Li*[b,†], *Yutong Ding*[a], *Tairong Kuang*[a,*]

[a] Functional Polymers & Advanced Materials (FPAM) Lab, State Key Laboratory of Advanced Separation Membrane Materials, Zhejiang Key Laboratory of Advanced Polymer Materials Modification and Application Technology, College of Materials Science and Engineering, Zhejiang University of Technology, Hangzhou 310014, Zhejiang, P. R. China

[b] Suzhou Laboratory, Suzhou 215123, Jiangsu, P. R. China

[†] These authors contributed equally to this work.

[*]*Corresponding author:* kuangtr@zjut.edu.cn (T. Kuang).

Supplementary Experimental Section

Molecular dynamics (MD) simulations

A coarse-grained (CG) model was developed to investigate the morphology evolution of PLA/PBS composite films containing multi-walled carbon nanotubes (CNTs). All simulations were performed using reduced Lennard–Jones (LJ) units, with unit length σ, mass m, energy ϵ, and time $\tau=\sqrt{m\sigma^2/\epsilon}$. PLA and PBS polymers were represented as bead-spring chains consisting of 20 and 10 CG beads, respectively. Each bead had a diameter of σ and mass m. Adjacent beads along a polymer chain were connected via a finitely extensible nonlinear elastic (FENE) bond potential,

$$U_{FENE}(r)=-0.5k_bR_0^2\ln\left(1-r^2/R_0^2\right),$$

where the spring constant was set to $k_b=30\epsilon/\sigma^2$ and the maximum bond extension to $R_0=1.5\sigma$. CNTs were modeled as rigid rod-like chains composed of 40 CG beads (mass m per bead). Chain connectivity was enforced using the same FENE potential, while rigidity was imposed by a harmonic potential,

$$U_{angle}(\theta)=k_\theta(\theta-\theta_0)^2,$$

where $k_\theta=300\epsilon$ and an equilibrium angle $\theta_0=180°$. The CNT diameter was set to 2σ, consistent with their relative size compared with polymer chains in the experimental system.

The thin-film simulation box contained 7,000 PLA chains and 6,000 PBS chains (PLA:PBS = 7:3 by bead number), with the number of CNTs varied from 0 to 300 to represent different loadings. The film thickness was fixed at $h=30\sigma$.

A generic force field was employed. Excluded-volume interactions were described by a purely repulsive Weeks–Chandler–Andersen (WCA) potential,

$$U_{WCA}(r_{ij})=\begin{cases}4\varepsilon_{WCA}\left[\left(\frac{\sigma}{r_{ij}}\right)^{12}-\left(\frac{\sigma}{r_{ij}}\right)^{6}+\frac{1}{4}\right], & r_{ij}\le 2^{1/6}\sigma\\ 0, & r_{ij}>2^{1/6}\sigma\end{cases}$$

where r_{ij} is the distance between beads i and j. Attractive interactions were modeled using the standard LJ potential,

$$U_{LJ}(r_{ij})=4\varepsilon_{LJ}\left[\left(\frac{\sigma}{r_{ij}}\right)^{12}-\left(\frac{\sigma}{r_{ij}}\right)^{6}\right],\ r_{ij}\leq 2.5\sigma.$$

PLA–PLA and PBS–PBS interactions were attractive, while all other non-bonded interactions were purely repulsive to promote phase separation. The LJ energy parameters (ε_{LJ}) for PLA and PBS were chosen to distinguish their relative domain softness, as summarized in Table S2. An enhanced repulsive interaction strength of $\varepsilon_{WCA}=4$ was applied between PLA and PBS to drive immiscibility. Thin film confinement along the z-direction was imposed using a 9-3 LJ wall potential applied at the top and bottom surfaces,

$$U_{wall}(r_{ij})=\left[\frac{2}{15}\left(\frac{\sigma}{r_{ij}}\right)^{9}-\left(\frac{\sigma}{r_{ij}}\right)^{3}\right],\ r_{ij}\leq 2.5\sigma.$$

Molecular dynamics simulations were performed to elucidate the effect of CNT loading on film morphology. The integration timestep was set to $\Delta t=0.005\tau$. A Langevin thermostat and a Berendsen barostat were used to control temperature (T) and lateral pressure (P), with damping parameters of 1τ and 5τ, respectively.

Initial configurations were generated by randomly placing polymer chains and CNTs inside a film (with a large initial lateral side length of $L=400\sigma$). To accelerate phase evolution, a thermal annealing protocol was applied, consisting of five heating-cooling cycles between $T=1.0$ and $T=3.0$ at a lateral pressure of $P=1.0$, with each cycle lasting 2×10^5 timesteps. The system was then equilibrated at $T=1.0$ and $P=0.0$ for 5×10^6 timesteps, followed by a production run of 2×10^6 timesteps.

All MD simulations were carried out using LAMMPS. Statistical analyses were averaged over five independent simulations initialized with different random configurations.

Supplementary Note

Supplementary Note S1: Calculation of interfacial polarization efficiency (η_{IP})

The interfacial polarization efficiency (η_{IP}) is introduced to quantitatively evaluate the polarization gain contributed per unit mass of conductive nanofiller. It is defined as:

$$\eta_{IP}=\frac{\varepsilon'(f_{low})}{\phi_{CNT}}$$

where $\varepsilon'(f_{low})$ is the dielectric constant measured at low frequency, and ϕ_{CNT} is the mass fraction of CNTs in the PLA/PBS composite (0.5, 1, 2, and 3 wt%). This metric allows direct comparison of interfacial polarization efficiency across different CNT loadings. The calculated η_{IP} values for all samples are summarized in Figure S15.

Supplementary Note S2: Trap characterization methods and calculations

Carrier traps, defined as localized energy states capable of capturing charge carriers, were quantitatively evaluated using the isothermal surface potential decay (ISPD) method. This technique records the temporal decay of surface-deposited charge under isothermal conditions, enabling extraction of trap energy levels and trap density distributions without external stimulation of trapped charge.[1]

In a typical ISPD measurement, the sample surface was first polarized for 5 min using a corona needle at an applied voltage of 15 kV. The sample was then rapidly transferred beneath a high-speed electrostatic probe (HVP40) to monitor the surface potential decay as a function of time.

The trap energy level E and trap density distribution $N_t(E)$ were calculated using the following relations:

$$E=k_BT\ In(\nu t)$$

$$N_t(E)=\frac{4\varepsilon_0\varepsilon_r}{qL^2k_BT}\left|t\frac{dV_S(t)}{dt}\right|$$

where $k_B=1.38\times10^{-23}$J/K is the Boltzmann constant, T is the measurement temperature (298K), and ν is the attempt-to-escape frequency of trapped charges

(taken as 10^{12} s^{-1}). L is the sample thickness, ε_0 is the vacuum permittivity, ε_r is the relative permittivity of the material, q is the elementary charge, and $V_S(t)$ is the time-dependent surface potential.

Using these equations, the distributions of trap depth and trap density were obtained, enabling quantitative analysis of charge capture, retention, and release behavior in the IMCA composites.

Supplementary Note S3: Calculation of material work function

The work function (Φ) of a material is defined as the minimum energy required to remove an electron from the material surface to vacuum. The sample work function (Φ_{Sample}) was determined using Kelvin probe force microscopy (KPFM) according to:

$$\Phi_{Sample} = \Phi_{Tip} - eV_{cpd}$$

where Φ_{Tip} is the work function of the conductive AFM probe tip (Au, 5.2 eV), e is the elementary charge, and V_{cpd} is the contact potential difference between the sample and the probe.

The contact potential difference is given by:

$$V_{cpd} = V_{Sample} - V_{Au}$$

where V_{Sample} is the measured surface potential of the sample relative to the probe, and V_{Au} is the surface potential of the Au reference relative to the probe. The potential difference between the Au reference and the probe was measured to be 0.0151 V.

All calculated work function values and relevant parameters are summarized in Table S5.

Supplementary Figures

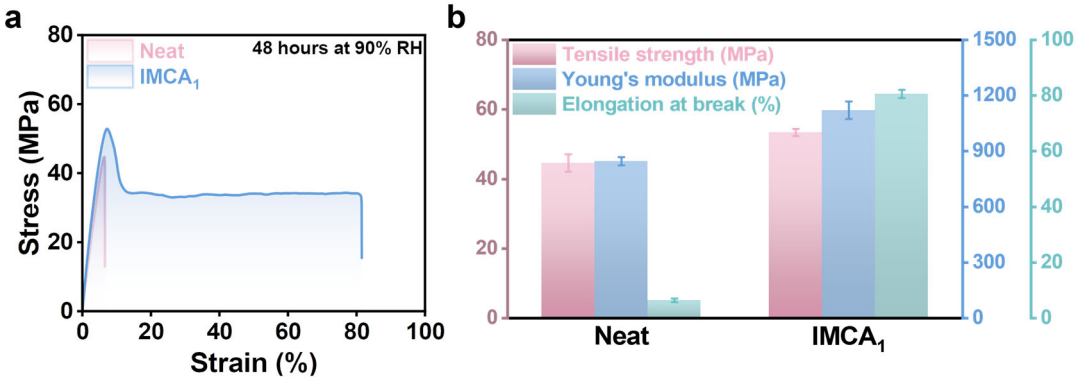

Supplementary Figure S1. Mechanical properties of neat PLA/PBS and IMCA$_1$ films after exposure to high humidity. (a) Stress-strain curves after exposure to 90% relative humidity (RH) for 48 h. (b) Comparison of tensile strength, Young's modulus and elongation at break after humidity exposure.

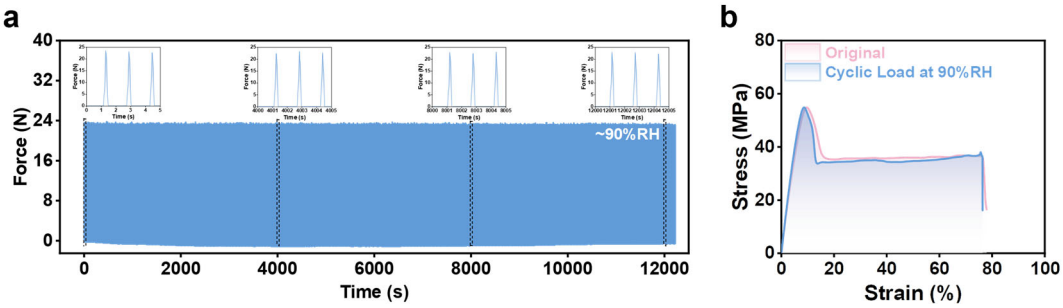

Supplementary Figure S2. Mechanical stability of IMCA$_1$ films under cyclic loading in a high-humidity environment. (a) Cyclic tensile loading–unloading behavior at 90% RH. (b) Stress-strain curves before and after cyclic stimulation.

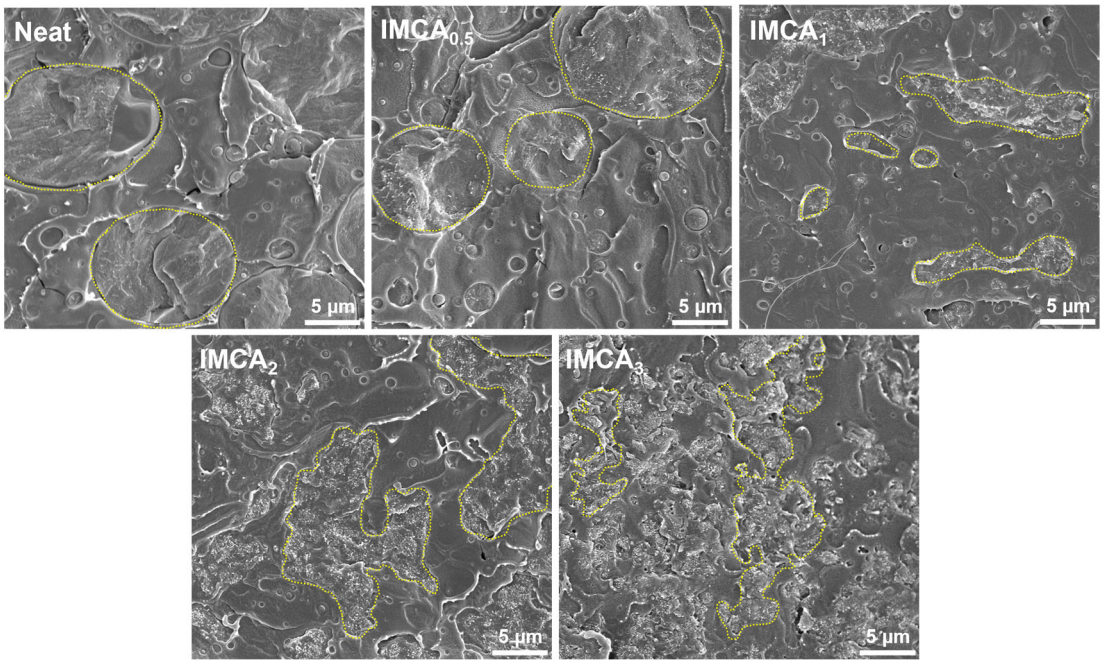

Supplementary Figure S3. Scanning electron microscopy (SEM) images of IMCA composites with different CNT loadings, illustrating CNT-induced phase morphology evolution.

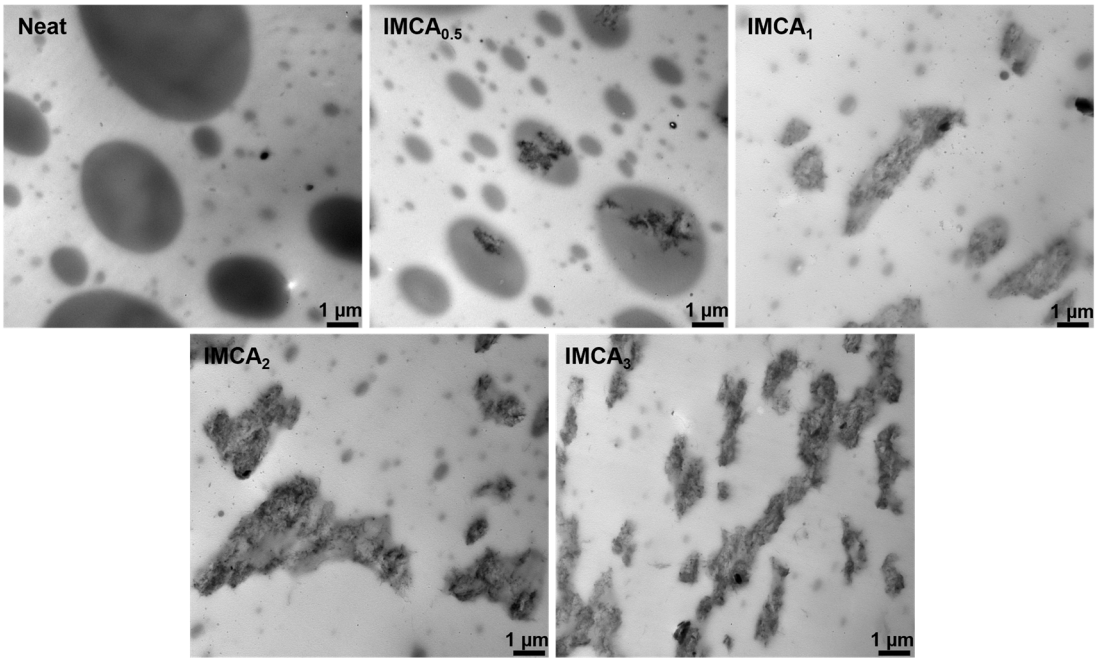

Supplementary Figure S4. Transmission electron microscopy (TEM) images of IMCA composites with different CNT loadings, revealing interfacial CNT localization and domain morphology.

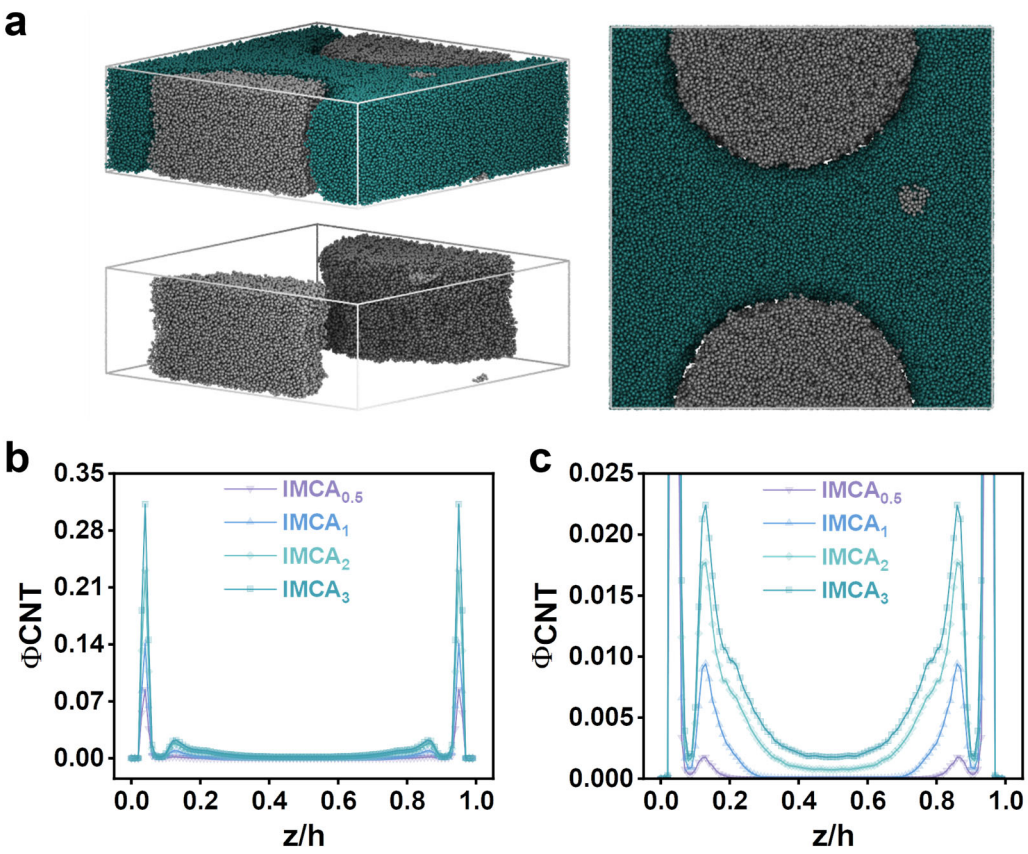

Supplementary Figure S5. Morphological characteristics of phase-separated polymer films obtained from coarse-grained MD simulations. (a) Simulation snapshots showing the phase-separated domain structure in the neat polymer blend. (b) CNT number density distribution along the film thickness (*z*) direction at different CNT loadings. (c) Enlarged CNT number density distribution highlighting CNT bridging between different interfacial regions at higher loadings (> 1 wt%).

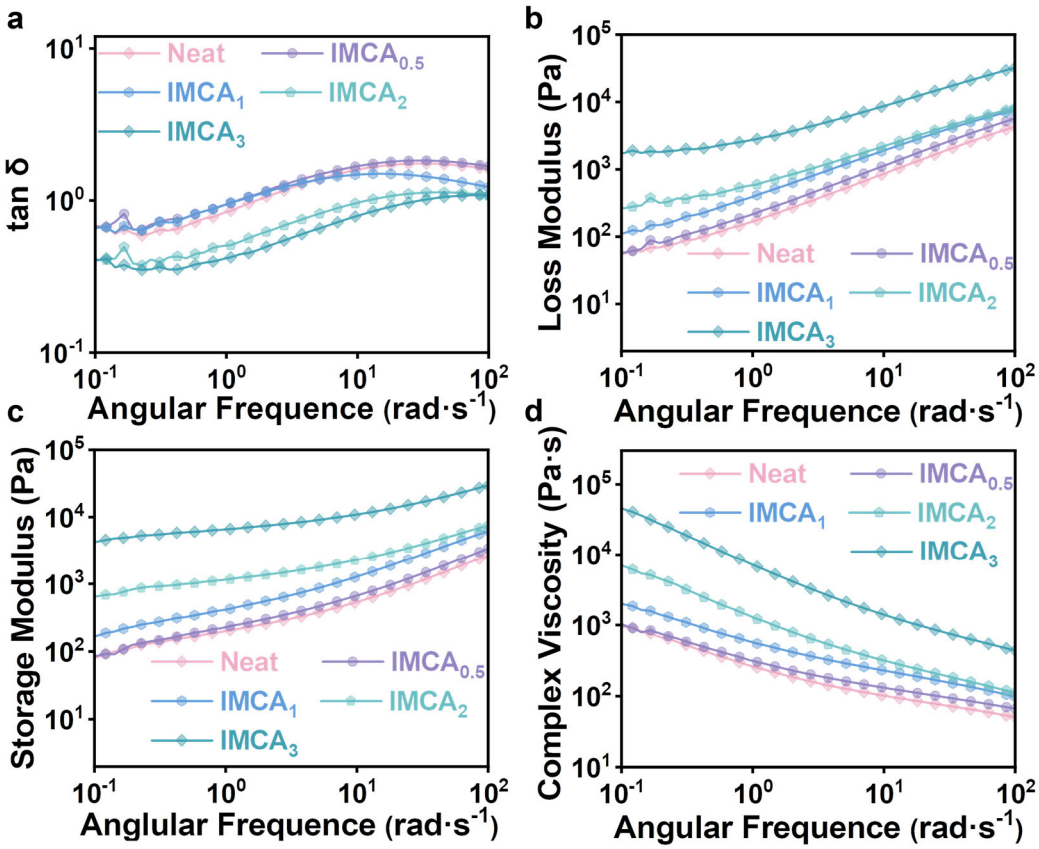

Supplementary Figure S6. Rheological properties of IMCA composites with varying CNT loadings: (a) loss tangent (Tan δ), (b) loss modulus, (c) storage modulus, and (d) complex viscosity.

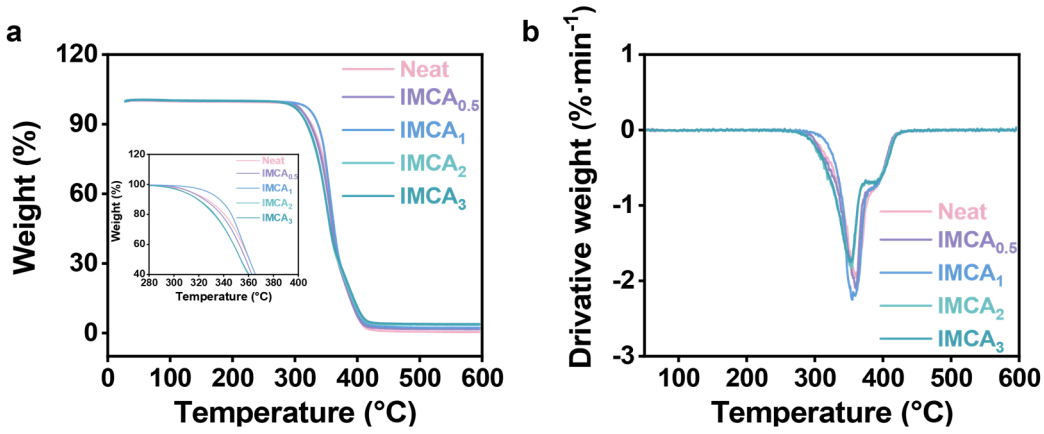

Supplementary Figure S7. Thermal properties of IMCA composites: (a) thermogravimetric analysis (TGA) curves and (b) differential thermal analysis (DTG) curves.

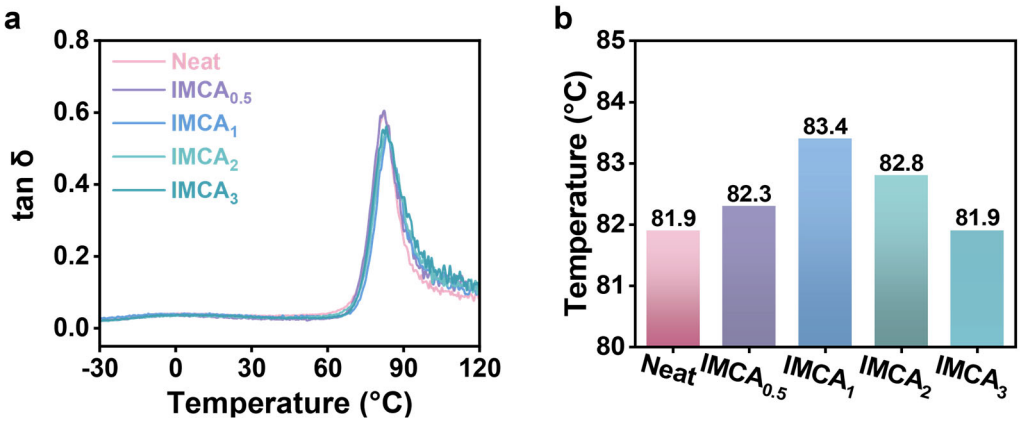

Supplementary Figure S8. Dynamic mechanical analysis (DMA) of IMCA composites: (a) temperature-dependent loss tangent (Tan δ) and (b) glass transition temperature (T_g) extracted from DMA measurements.

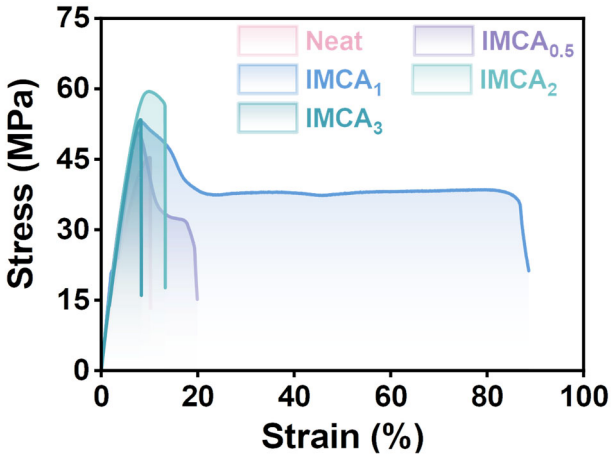

Supplementary Figure S9. Stress-strain curves of IMCA composites with different CNT loadings.

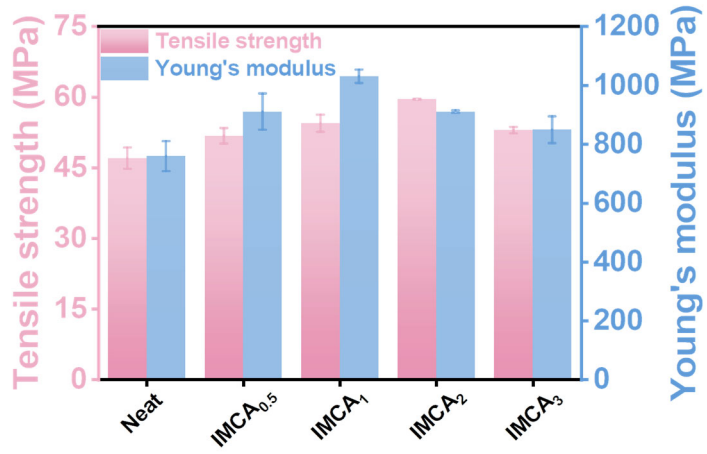

Supplementary Figure S10. Tensile strength and Young's modulus of IMCA composites at different CNT loadings.

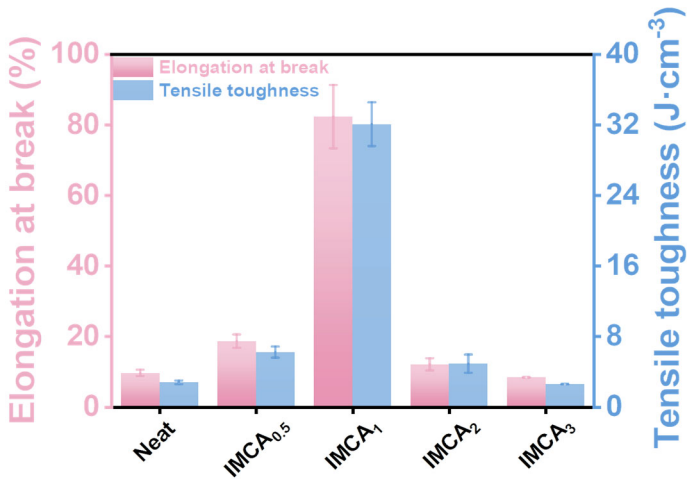

Supplementary Figure S11. Elongation at break and tensile toughness of IMCA composites at different CNT loadings.

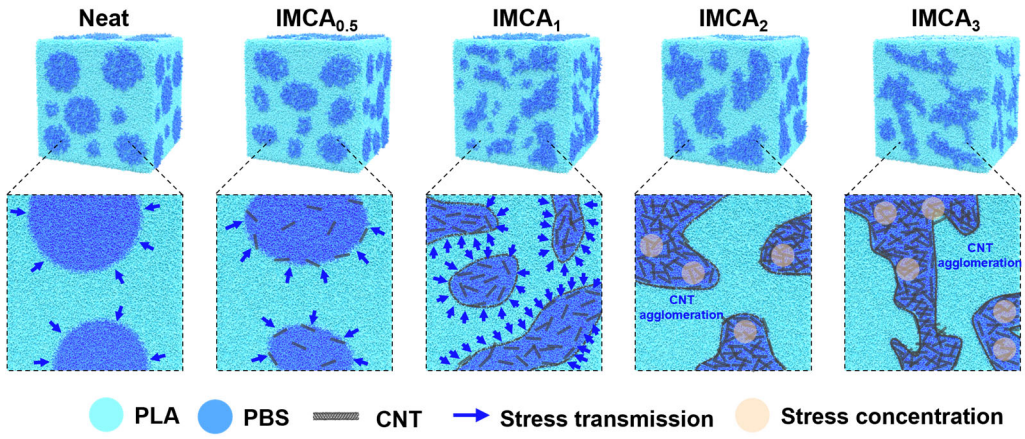

Supplementary Figure S12. Schematic illustration of interfacial stress-transfer mechanisms in IMCA composites at different CNT loadings.

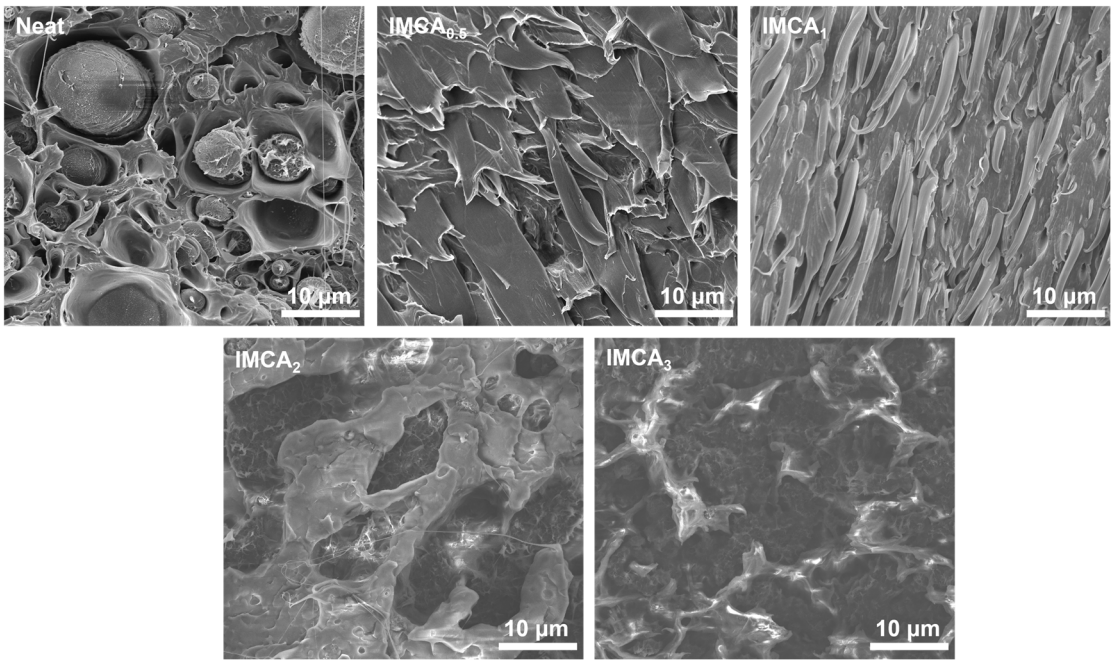

Supplementary Figure S13. SEM images of tensile fracture surfaces of IMCA composites with different CNT loadings.

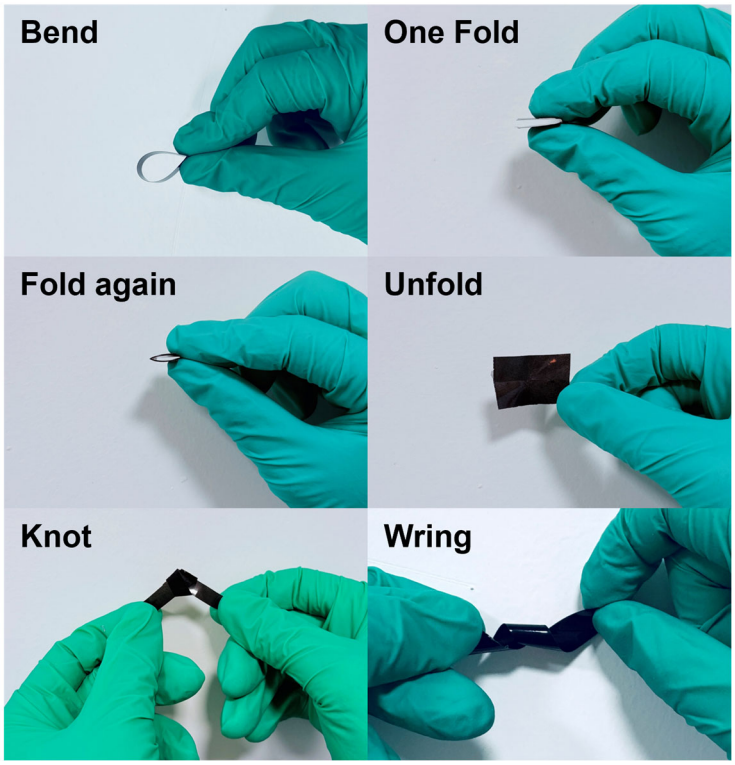

Supplementary Figure S14. Photographs demonstrating the mechanical flexibility of $IMCA_1$ composite film.

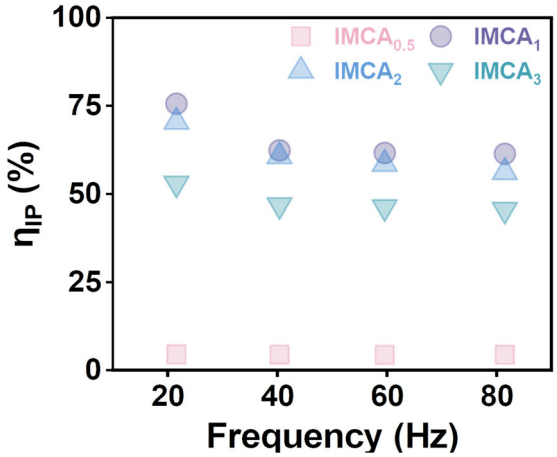

Supplementary Figure S15. Interfacial polarization efficiency (η_{IP}) of IMCA composites with different CNT loadings.

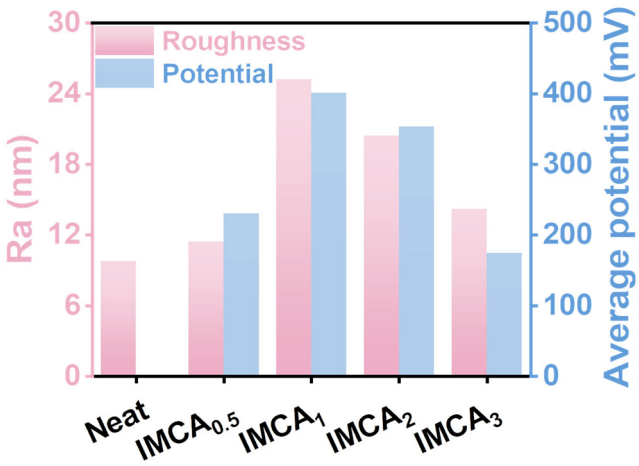

Supplementary Figure S16. Surface roughness and average potential of IMCA composites measured by atomic force microscopy and Kelvin probe force microscopy.

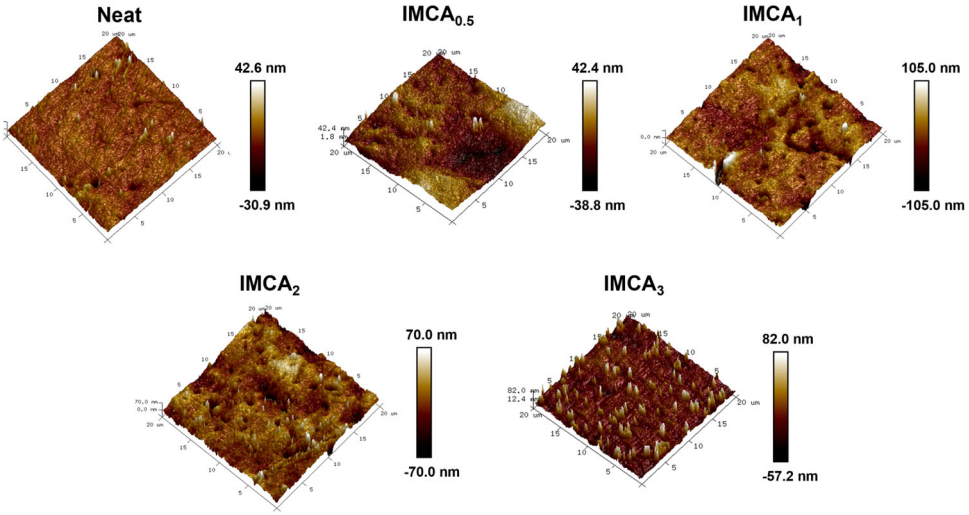

Supplementary Figure S17. Three-dimensional AFM topography images of IMCA composites with different CNT loadings.

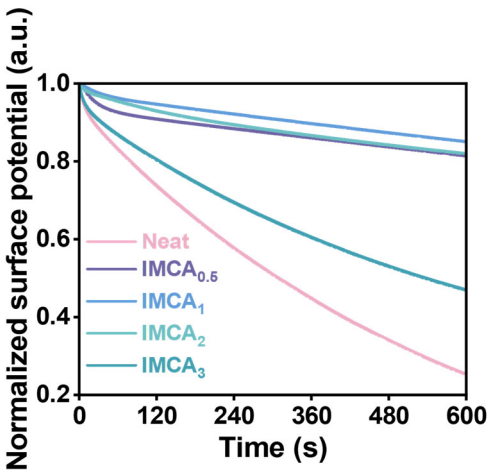

Supplementary Figure S18. Normalized surface potential decay curves of IMCA composites obtained from isothermal surface potential decay (ISPD) measurements.

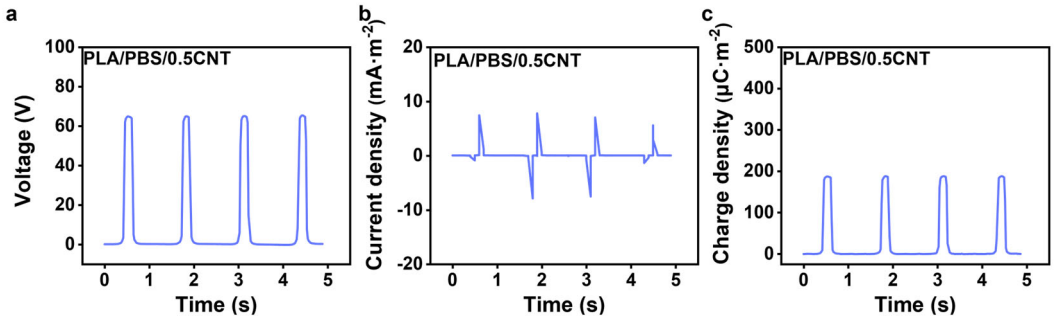

Supplementary Figure S19. Triboelectric output performance of PLA/PBS/0.5CNT-based TENGs: (a) open-circuit voltage, (b) current density, and (c) surface charge density.

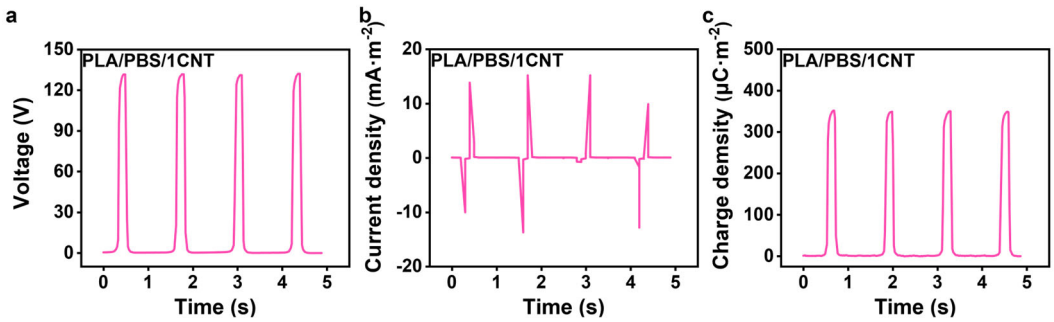

Supplementary Figure S20. Triboelectric output performance of PLA/PBS/1CNT-based TENGs: (a) open-circuit voltage, (b) current density, and (c) surface charge density.

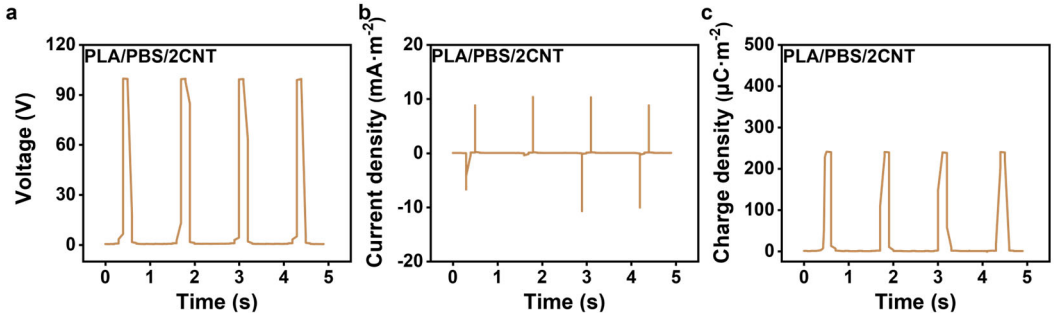

Supplementary Figure S21. Triboelectric output performance of PLA/PBS/2CNT-based TENGs: (a) open-circuit voltage, (b) current density, and (c) surface charge density.

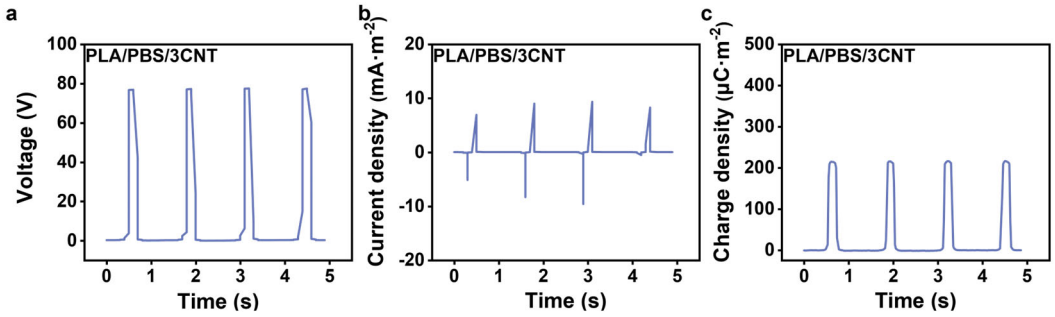

Supplementary Figure S22. Triboelectric output performance of PLA/PBS/3CNT-based TENGs: (a) open-circuit voltage, (b) current density, and (c) surface charge density.

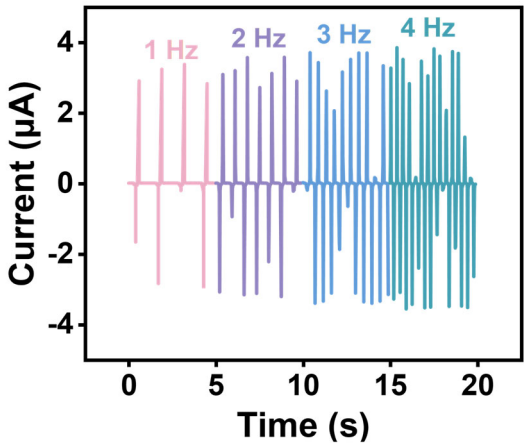

Supplementary Figure S23. Short-circuit current of the $IMCA_1$ C-TENG at different operating frequencies.

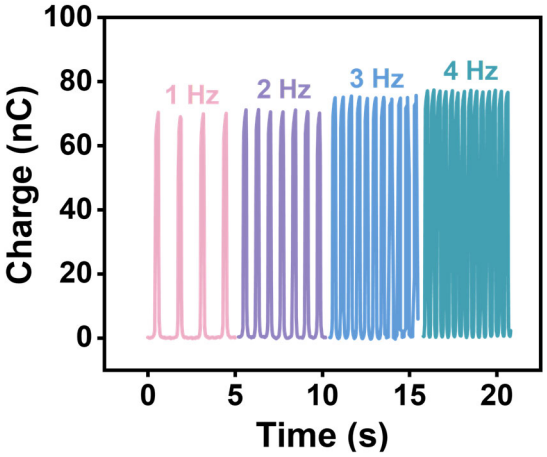

Supplementary Figure S24. Transferred charge of the $IMCA_1$ C-TENG at different operating frequencies.

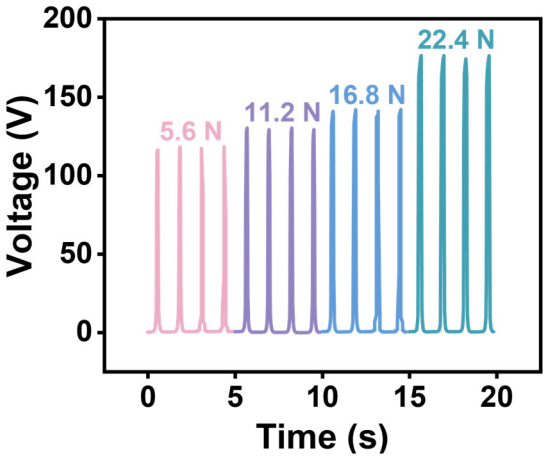

Supplementary Figure S25. Output voltage of the $IMCA_1$ C-TENG under different applied normal forces.

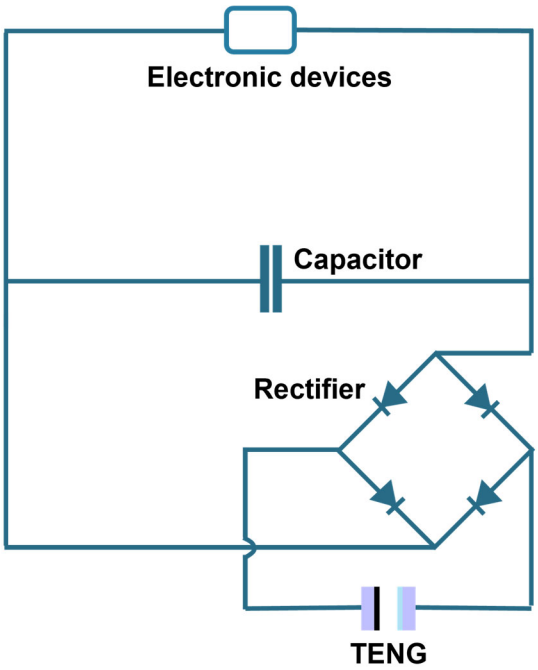

Supplementary Figure S26. Circuit diagram of the full-wave bridge rectifier used for energy storage measurements.

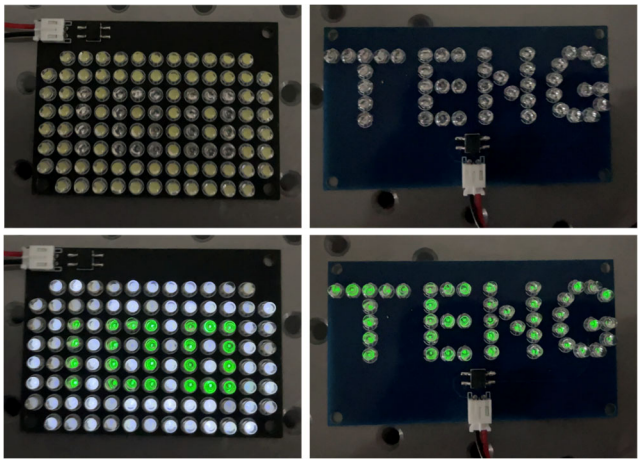

Supplementary Figure S27. Photographs demonstrating the IMCA$_1$ C-TENG directly powering LEDs.

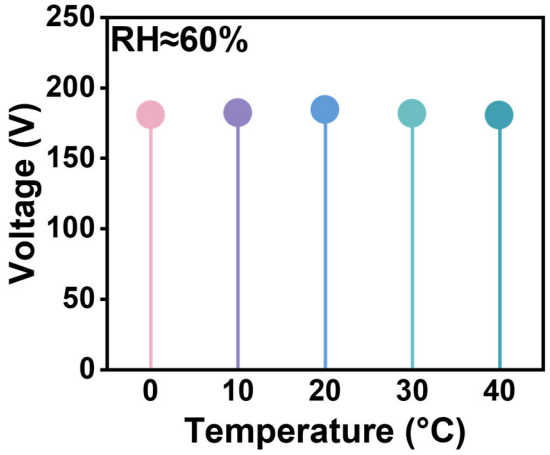

Supplementary Figure S28. Open-circuit voltage of the $IMCA_1$ C-TENG measured at different temperatures.

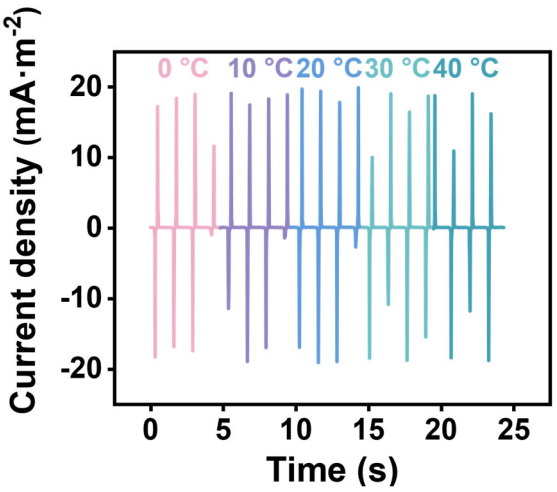

Supplementary Figure S29. Current density of the $IMCA_1$ C-TENG measured at different temperatures.

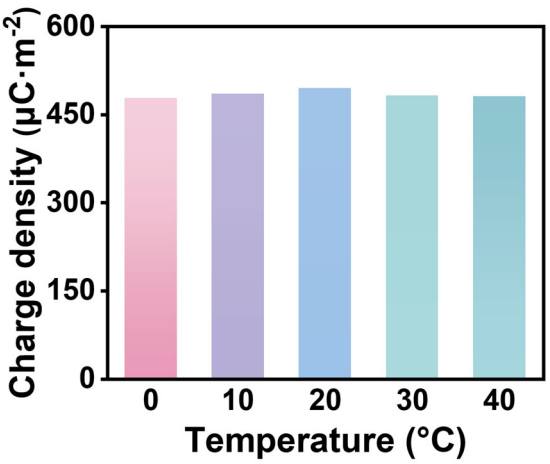

Supplementary Figure S30. Surface charge density of the $IMCA_1$ C-TENG measured at different temperatures.

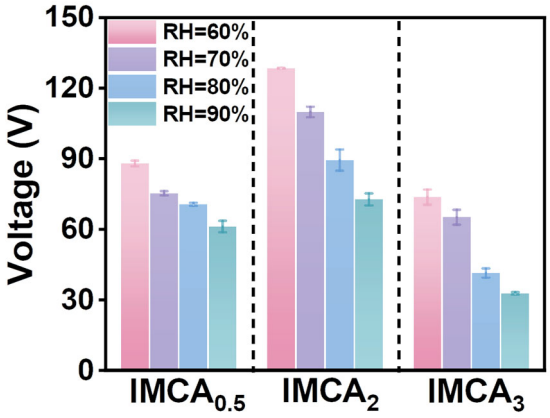

Supplementary Figure S31. Open-circuit voltage of $IMCA_x$ composites (x=0.5, 2, and 3 wt% CNT) measured under different relative humidity conditions.

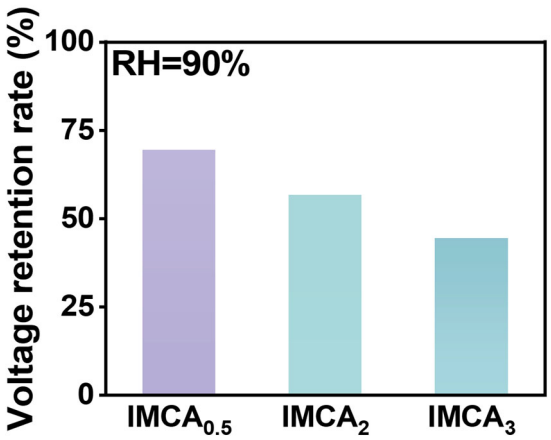

Supplementary Figure S32. Voltage retention of IMCA$_x$ composites (x=0.5, 2, and 3 wt% CNT) during prolonged operation at 90% RH.

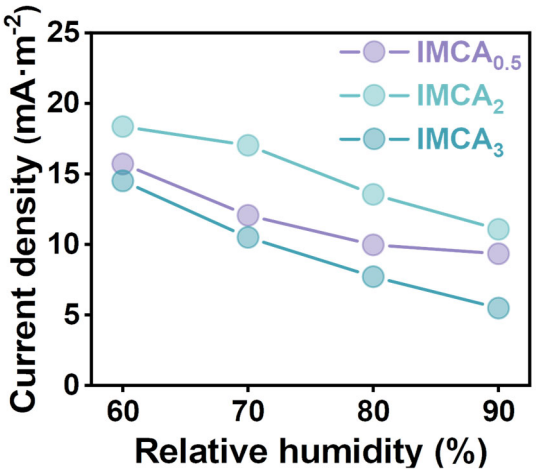

Supplementary Figure S33. Current density of IMCA$_x$ composites (x=0.5, 2, and 3 wt% CNT) measured under different relative humidity conditions.

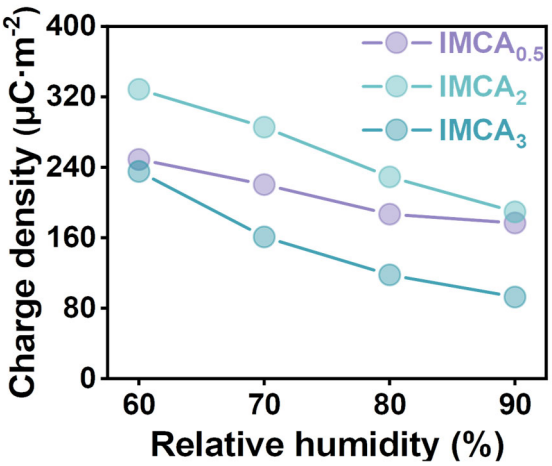

Supplementary Figure S34. Surface charge density of IMCA$_x$ composites (x=0.5, 2, and 3 wt% CNT) measured under different relative humidity conditions.

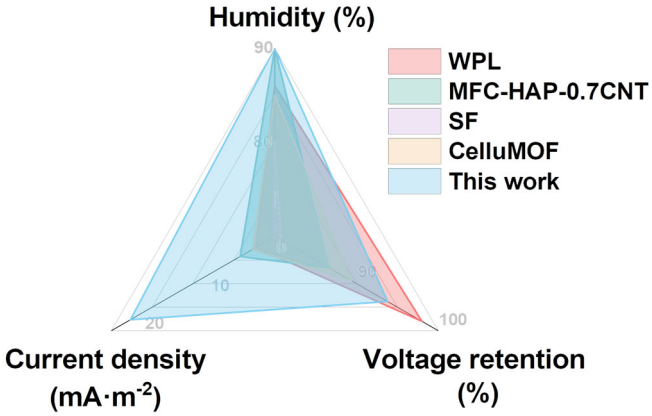

Supplementary Figure S35. Comparison of the humidity tolerance and electrical output of the IMCA$_1$ C-TENG with representative hydrophobic surface-modified TENGs in the literature.

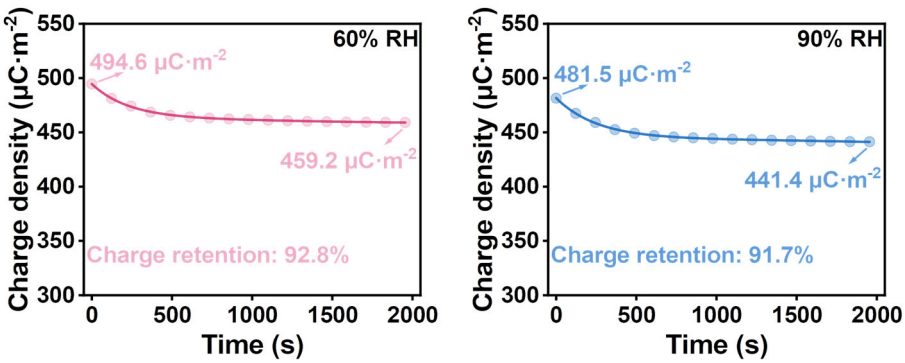

Supplementary Figure S36. Surface-charge decay kinetics of the IMCA$_1$ composite film measured at (a) 60% RH and (b) 90% RH.

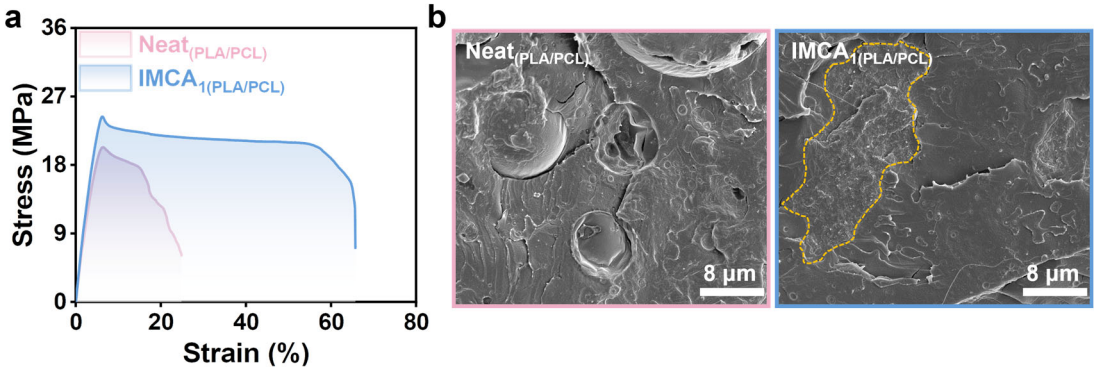

Supplementary Figure S37. (a) Mechanical properties and (b) SEM images of $Neat_{(PLA/PCL)}$ and $IMCA_{1(PLA/PCL)}$.

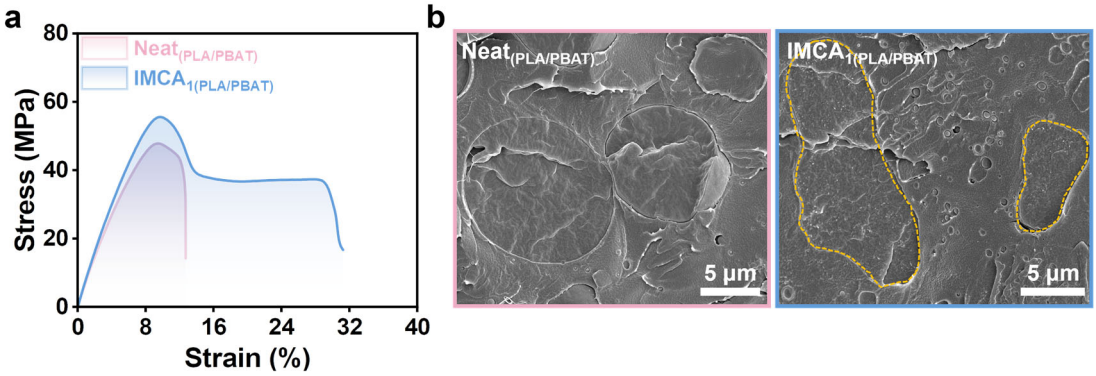

Supplementary Figure S38. (a) Mechanical properties and (b) SEM images of $Neat_{(PLA/PBAT)}$ and $IMCA_{1(PLA/PBAT)}$.

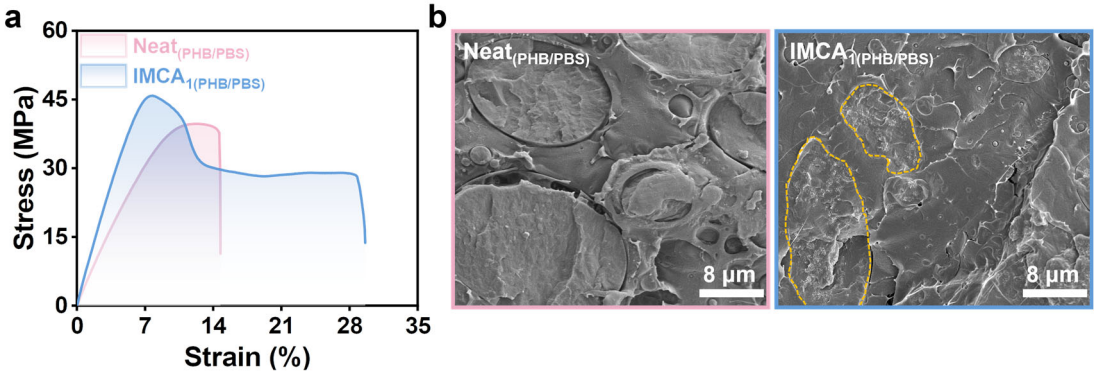

Supplementary Figure S39. (a) Mechanical properties and (b) SEM images of $Neat_{(PHB/PBS)}$ and $IMCA_{1(PHB/PBS)}$.

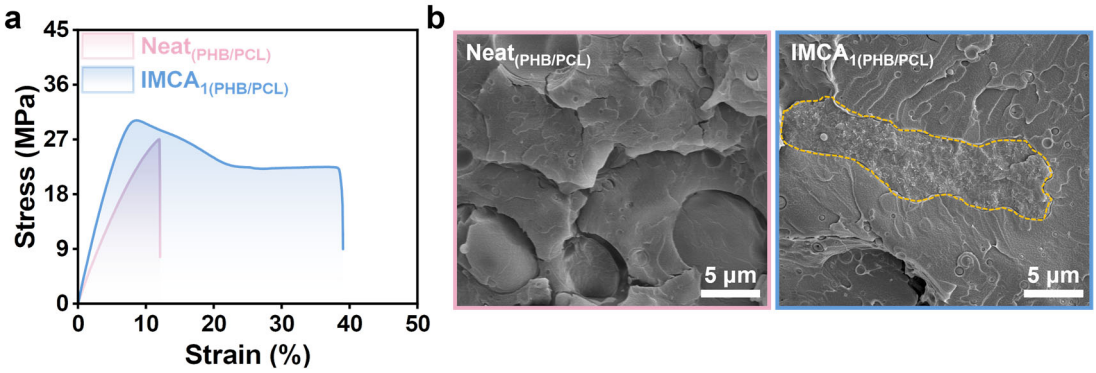

Supplementary Figure S40. (a) Mechanical properties and (b) SEM images of Neat$_{(PHB/PCL)}$ and IMCA$_{1(PHB/PCL)}$.

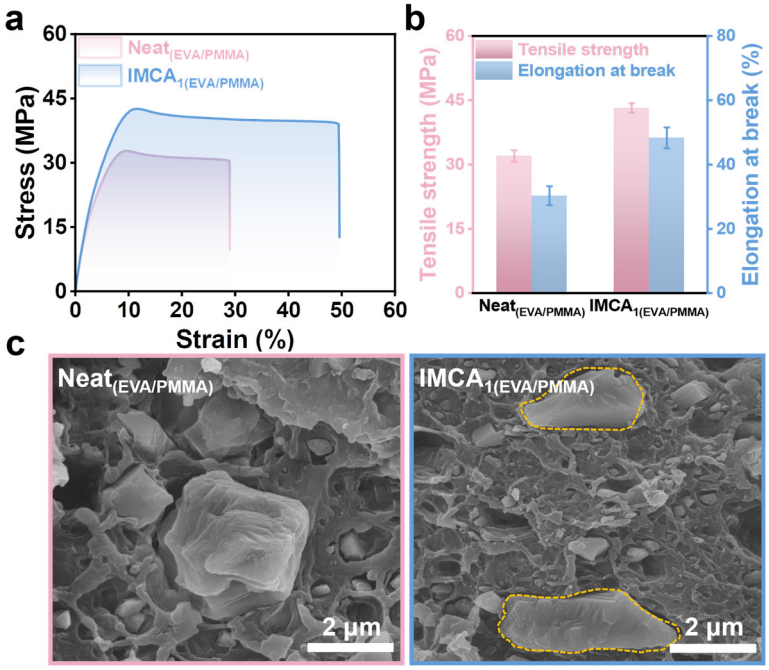

Supplementary Figure S41. (a) Mechanical properties, (b) tensile strength and elongation at break, and (c) SEM images of Neat$_{(EVA/PMMA)}$ and IMCA$_{1(EVA/PMMA)}$.

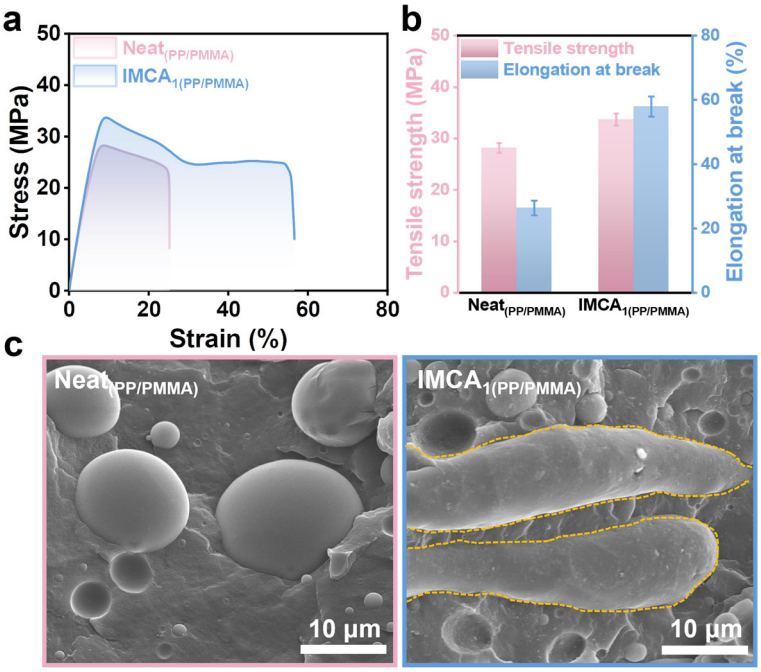

Supplementary Figure S42. (a) Mechanical properties, (b) tensile strength and elongation at break, and (c) SEM images of Neat(PP/PMMA) and IMCA1(PP/PMMA).

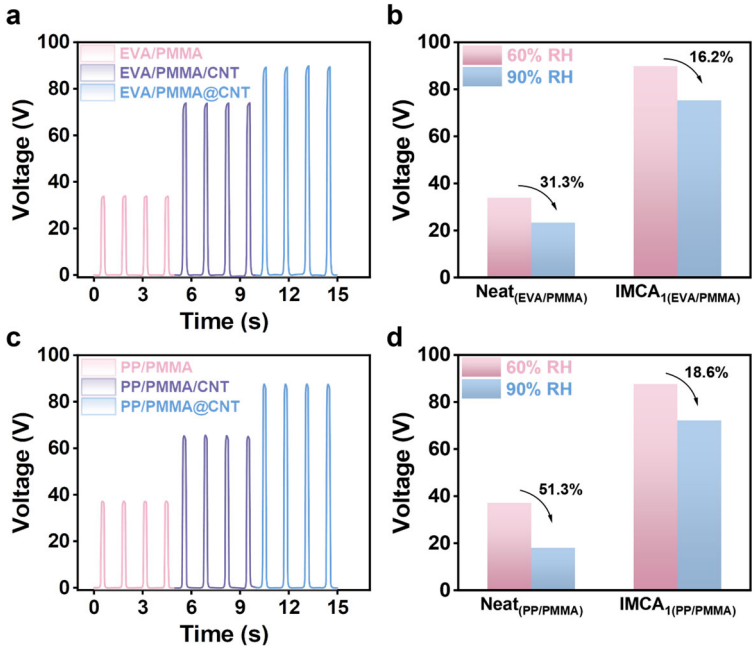

Supplementary Figure S43. Triboelectric output performance of non-bio-based immiscible polymer systems: (a) Open-circuit voltage of EVA/PMMA, EVA/PMMA/CNT (randomly dispersed), and EVA/PMMA@CNT (interfacially confined). (b) Output voltage of Neat(EVA/PMMA) and IMCA1(EVA/PMMA) measured at 60% and 90% RH. (c) Open-circuit voltage of PP/PMMA, PP/PMMA/CNT (randomly dispersed), and PP/PMMA@CNT (interfacially confined). (d) Output voltage of Neat(PP/PMMA) and IMCA1(PP/PMMA) at 60% and 90% RH.

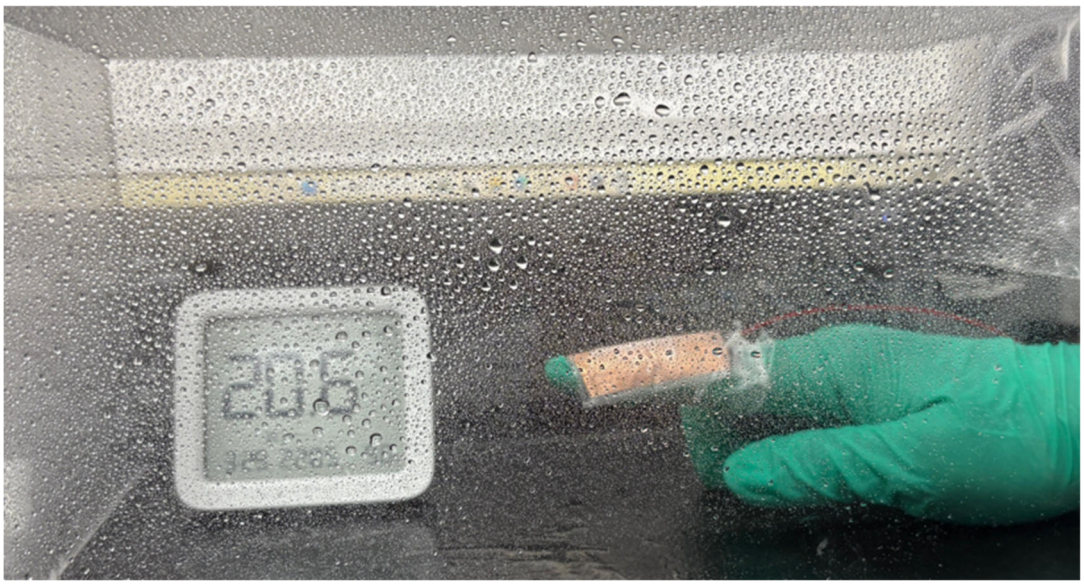

Supplementary Figure S44. Photographs of flexible sensors based on $IMCA_1$ C-TENG operating under high-humidity conditions (RH≈90%).

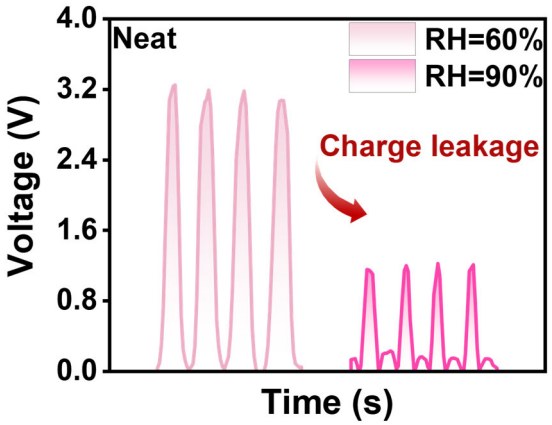

Supplementary Figure S45. Output voltage signals of flexible sensors based on neat polymer film measured at 60% and 90% RH.

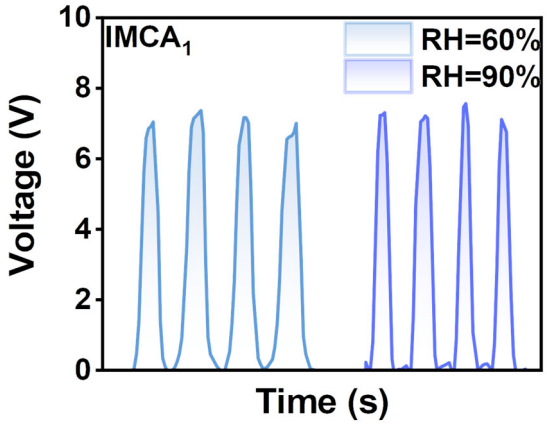

Supplementary Figure S46. Output voltage signals of flexible sensors based on $IMCA_1$ composite film measured at 60% and 90% RH.

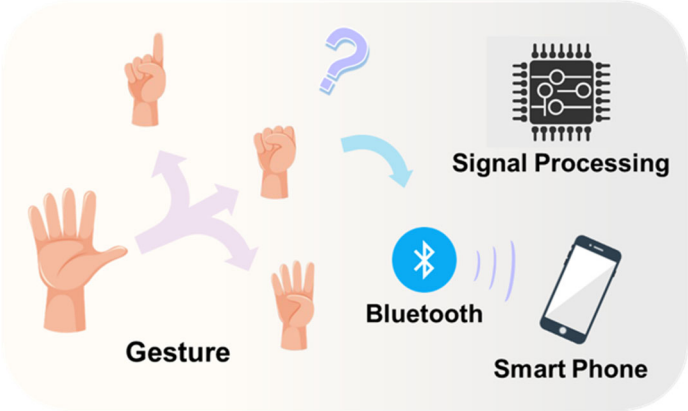

Supplementary Figure S47. Schematic illustration of the signal transmission principle for gesture recognition.

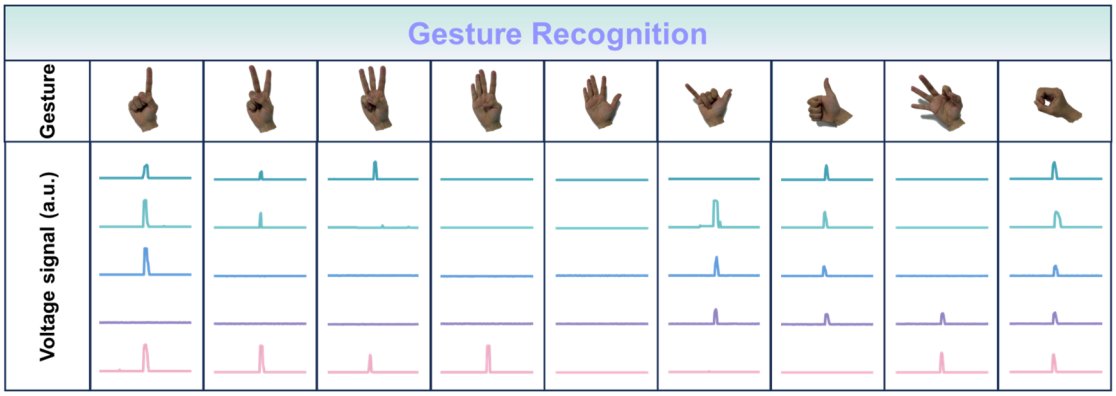

Supplementary Figure S48. Voltage output signals corresponding to different hand gestures detected by the $IMCA_1$ C-TENG-based flexible sensor.

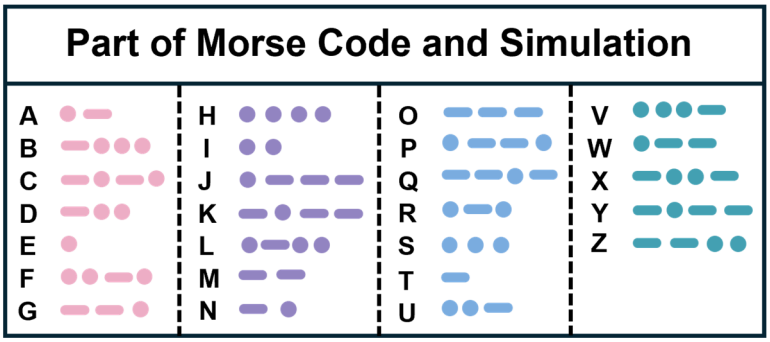

Supplementary Figure S49. International Morse code reference table used for signal encoding and decoding.

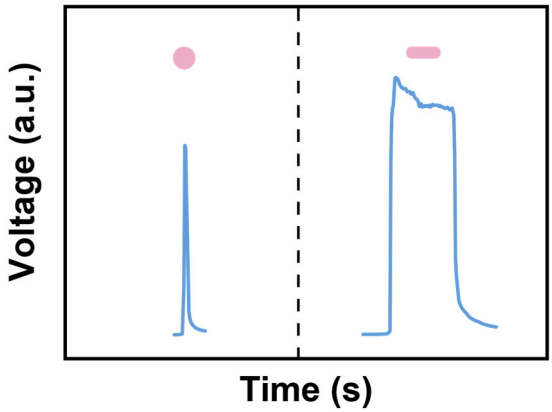

Supplementary Figure S50. Morse code signals generated by the IMCA$_1$ C-TENG.

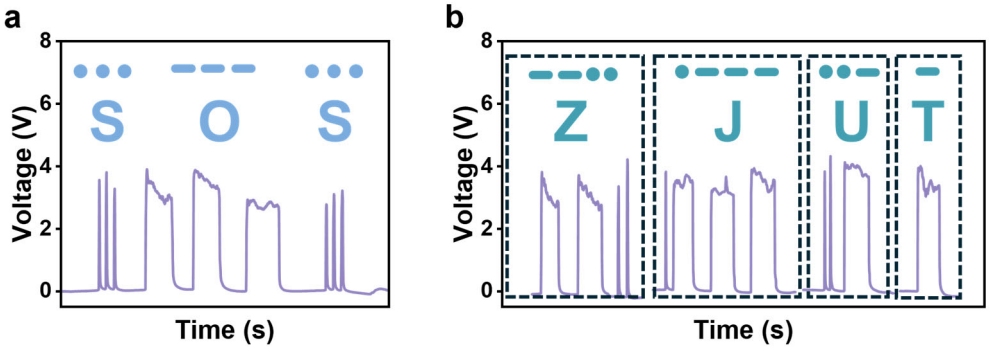

Supplementary Figure S51. Electrical output signals corresponding to the Morse code messages “SOS” and “ZJUT” generated by the IMCA$_1$ C-TENG.

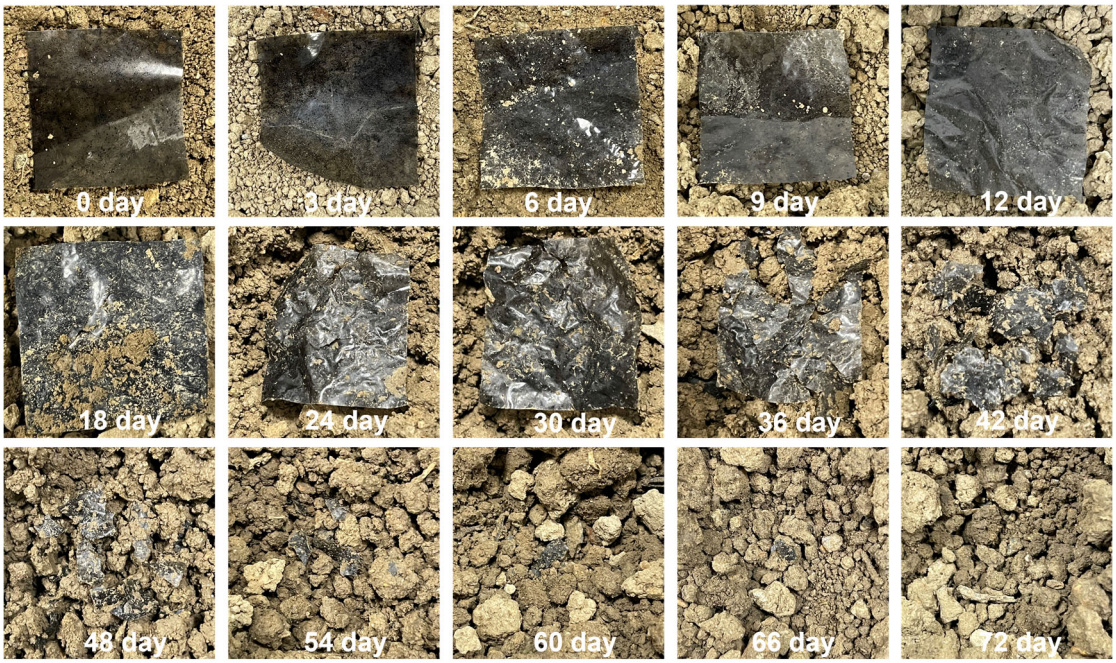

Supplementary Figure S52. Photographs showing the soil-degradation behavior of IMCA$_1$ composite film at different degradation stages.

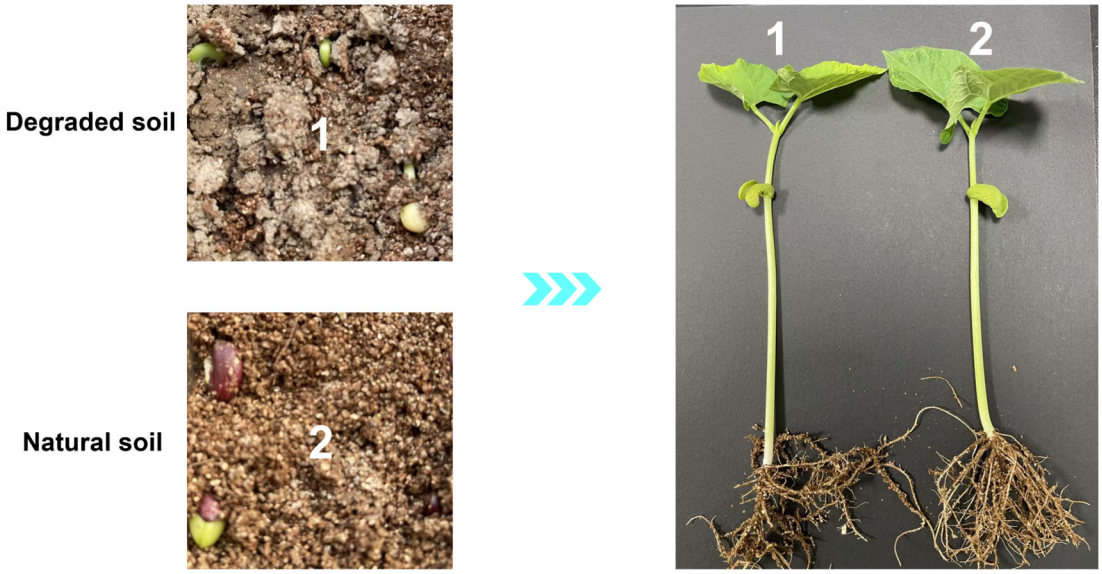

Supplementary Figure S53. Photographs of kidney bean seed growth in soil containing degraded IMCA$_1$ film and in natural soil, demonstrating ecological compatibility.

Supplementary Tables

Table S1. Comparison of moisture stability, triboelectric output performance, and mechanical properties of representative eco-friendly TENGs reported in the literature.

Materials	**Moisture Stability (%)**	**Charge density ($\mu C \cdot m^{-2}$)**	**Power density ($mW \cdot m^{-2}$)**	**Elongation at break enhancement (folds)**	**Tensile strength (MPa)**	**Ref.**
C5E20	84.6	280.0	200.0	1.2	60.6	2
p-N_3BMA-AA	76	456.0	464.0	1.9	0.2	3
Cellulose/$PEI_{1.5\%}$	36.4	18.9	145.9	2.6	23.8	4
WPU	78.8	33.3	0.08	1.1	27.9	5
GLCL	92	231.0	203.1	1.3	1.5	6
$IMCA_1$	**93.8**	**496.1**	**968.5**	**8.6**	**54.4**	**This work**

Table S2. Force-field parameters used in molecular dynamics (MD) simulations.

	PLA	**PBS**	**CNT**
PLA	ε_{LJ}=1.2	ε_{WCA}=4	ε_{WCA}=1
PBS	ε_{WCA}=4	ε_{LJ}=0.8	ε_{WCA}=1
CNT	ε_{WCA}=1	ε_{WCA}=1	ε_{WCA}=1

Table S3. Thermal stability parameters of IMCA composites with different phase structures.

Sample	$T_{d5\%}$ (℃)	$T_{d50\%}$ (℃)	DTG peak (℃)
Neat	313.6	360.5	359.7
$IMCA_{0.5}$	313.5	357.8	360.4
$IMCA_1$	327.4	360.6	355.2
$IMCA_2$	308.2	353.5	354.0
$IMCA_3$	308.1	353.9	353.1

Table S4. Mechanical properties of IMCA composites with different CNT loadings.

Sample	Tensile strength (MPa)	Young's modulus (MPa)	Elongation at break (%)
Neat	47.0±2.3	758.6±51.0	9.6±0.9
$IMCA_{0.5}$	51.7±1.6	910.0±61.5	18.6±1.9
$IMCA_1$	54.4±1.8	1030.3±23.0	82.3±9.0
$IMCA_2$	59.5±0.1	910.0±4.5	12.0±1.7
$IMCA_3$	52.9±0.7	848.4±45.7	8.3±0.1

Table S5. Parameters and calculated values used for work-function determination.

Sample	**V_{Sample}(V)**	**V_{cpd}(V)**	**Φ_{sample}(eV)**
Neat	0.000001	-0.151	5.351
$IMCA_{0.5}$	0.230	0.215	4.985
$IMCA_1$	0.401	0.386	4.814
$IMCA_2$	0.353	0.338	4.862
$IMCA_3$	0.174	0.159	5.041

Table S6. Comparison of long-term output stability of the $IMCA_1$ C-TENG and previously reported biopolymer-based TENGs.

Materials	**Voltage (V)**		**Ref.**
PEO/PGG-PCL/EC	0 s	6000 s	7
	6.3	6.3	
Functionalized wood	0 s	10000 s	8
	53.0	55.0	
SA/glycerol	0 s	3000 s	9
	84.0	83.0	
PLMBE/CNTs	0 s	800 s	10
	40.0	42.0	
HAP	0 s	5000 s	11
	110.0	100.1	
PLA/PBS/0.4MNPs	0 s	3000 s	12
	115.0	115.0	
GC-paper	0 s	10000 s	13
	160.0	155.0	
$IMCA_1$	**0 s**	**12200 s**	**This work**
	184.9	**184.2**	

Table S7. Comparison of output voltage of humidity-resistant wearable TENGs under different relative humidity conditions.

Materials	**Voltage (V)**				**Ref.**
SCGC	RH=60%	RH=70%	RH=80%	RH=90%	14
	160.0	130.0	110.0	95.0	
F-TENG	RH=55%	RH=75%		RH=95%	15
	45.0	32.0		29.0	
HPC	RH=65%	RH=75%		RH=85%	16
	170.0	150.0		105.0	
CA-PU-NH_2	RH=50%	RH=70%		RH=90%	17
	150.0	90.0		45.0	
FR-TENG	RH=55%	RH=58%	RH=68%	RH=72%	18
	100.0	95.0	80.0	75.0	
p-N3BMA-AA	RH=60%	RH=70%	RH=80%	RH=90%	3
	112.0	113.0	100.0	80.0	
$IMCA_1$	**RH=60%**	**RH=70%**	**RH=80%**	**RH=90%**	**This work**
	184.5	**182.1**	**181.5**	**173.1**	

Table S8. Comparison of test humidity, voltage retention, and current density for representative hydrophobic surface-modified TENGs reported in the literature.

Materials	**Humidity (%)**	**Voltage retention (%)**	**Current density ($mA \cdot m^{-2}$)**	**Ref.**
WPL	86.0	98.0	2.9	19
MFC-HAP-0.7CNT	90.0	86.6	5.3	20
SF	80.0	80.8	0.13	21
CelluMOF	85.0	89.4	3.4	22
$IMCA_1$	**90.0**	**93.8**	**22.1**	**This work**

References

1 J. He, T. Lyu, D. Song, Z. Song, X. Fan, X. Peng, L. Chen and K. Dong, *Adv. Mater.*, 2025, **37**, e10157.

2 T. Kuang, J. Zhang, G.-M. Huang, T. Liu and Z.-X. Huang, *Nano Energy*, 2024, **128**, 109877.

3 Y. Ding, H. Guo, M. Ouyang, G. Meng, F. Chen and T. Kuang, *Adv. Funct. Mater.*, 2025, **35**, 2421164.

4 C. Jiao, C. Li, J. Yue, L. Li, H. Yang, Y. Tao, J. Lu, Y. Lv, H. Wang, M. Tan and J. Du, *Nano Energy*, 2024, **122**, 109311.

5 A. Shi, B. Luo, W. Liu, W. Chen, Z. Li, S. Wang, L. Jiang, H. Zhang, X. Qin and W. Sun, *Adv. Mater.*, 2025, **37**, 2420459.

6 S. Sun, S. Hao, Y. Liu, S. Sun, Y. Xu, M. Jiang, C. Shao, J. Wen and R. Sun, *ACS Nano*, 2025, **19**, 811–825.

7 C. Li, R. Luo, Y. Bai, J. Shao, J. Ji, E. Wang, Z. Li, H. Meng and Z. Li, *Adv. Funct. Mater.*, 2024, **34**, 2400277.

8 Q. Jia, S. Xu, C. Wang, D. Zhang, K. Zhang, C. Lu, Q. Yong, J. Wang and F. Chu, *Nano Energy*, 2024, **129**, 109981.

9 Q. Feng, Z. Xie, Y. Wen, Z. Cheng, M. Zhang, Y. Wang, D. Liu, Y. Cao, Y. Mao and C. Zhao, *Sustain. Mater. Technol.*, 2025, **43**, e01262.

10 H. Wang, Y. Yin, Z. Su, C. Chen, L. Zhang, C. Wang, W. Yang, Y. Huang, P. Xu, P. Ma, T. Liu and P. Ma, *Adv. Funct. Mater.*, 2024, **34**, 2311649.

11 S. Liu, W. Tong, C. Gao, X. Wang, Y. Liu and Y. Zhang, *Chem. Eng. J.*, 2024, **493**, 152597.

12 C. Pei, H. Zhang, Y. Li, Z. Gu, X. Chen and T. Kuang, *Nano Energy*, 2025, **135**, 110643.

13 H. Liu, Q. Shu, H. Xiang, H. Wu, Z. Li and H. Zhou, *Nano Energy*, 2023, **108**, 108223.

14 X. Bo, W. Li, A. Valencia, H. Zhao, A. Budisuharto and W. A. Daoud, *Nano Energy*, 2024, **119**, 109085.

15 M. Feng, Y. Feng, J. Cheng, Z. Zhang, D. Yang, C. Du and D. Wang, *Nano Energy*, 2024, **127**, 109721.

16 J. He, Y. Xue, H. Liu, J. Li, Q. Liu, Y. Zhao, L. Mu, C.-L. Sun and M. Qu, *ACS Appl. Mater. Interfaces*, 2023, **15**, 43963–43975.

17 J. Shen, Z. Li, J. Yu and B. Ding, *Nano Energy*, 2017, **40**, 282–288.

18 R. Wang, J. Ma, S. Ma, Q. Zhang, N. Li, M. Ji, T. Jiao and X. Cao, *Chem. Eng. J.*, 2022, **450**, 137985.

19 R. Sun, Y. Wang, X. Li, Y. Li, K. Yang, H. Li, L. Jin, H. Zhu and F. Zhang, *ACS Appl. Electron. Mater.*, 2025, **7**, 4133–4143.

20 Y. Zhu, C. Feng, C. Jin, J. Cai, J. Huang, H. Na and J. Zhu, *Chem. Eng. J.*, 2025, **524**, 169377.

21 K. Chen, Y. Li, G. Yang, S. Hu, Z. Shi and G. Yang, *Adv. Funct. Mater.*, 2023, **33**, 2304809.

22 Z. Wu, C. Cai, X. Meng, Y. Liu, T. Liu and Z. Zhao, *Adv. Funct. Mater.*, 2026, **36**, e14745.